THE JOURNAL OF BIOLOGICAL CHEMISTRY Vol. 276, No. 13, Issue of March 30, pp. 9679–9687, 2001
*Printed in U.S.A.*

# Rotavirus Nonstructural Protein NSP2 Self-assembles into Octamers That Undergo Ligand-induced Conformational Changes*

Received for publication, October 16, 2000, and in revised form, November 29, 2000
Published, JBC Papers in Press, December 19, 2000, DOI 10.1074/jbc.M009398200

**Peter Schuck‡, Zenobia Taraporewala§, Peter McPhie¶, and John T. Patton§‖**

*From the ‡Division of Bioengineering and Physical Science, ORS, OD, ¶Laboratory of Biochemistry and Genetics, NIDDK, and §Laboratory of Infectious Diseases, NIAID, National Institutes of Health, Bethesda, Maryland 20892*

**The nonstructural protein NSP2 is a component of the rotavirus replication machinery and binds single-stranded RNA cooperatively, with high affinity, and independent of sequence. Recently, NSP2 has been shown to form multimers and to possess an NTPase activity, but its precise function remains unclear. In the present study, we have characterized the solution structure of recombinant NSP2 by velocity and equilibrium ultracentrifugation, dynamic light scattering, and circular dichroism spectroscopy. We found that NSP2 exists as an octamer, which is functional in the binding of RNA and ADP. In the presence of magnesium, a partial dissociation of the octamer into smaller oligomers was observed. This was reversed by binding of ADP and RNA. We observed an increased sedimentation rate in the presence of ADP and a nonhydrolyzable ATP analogue, which suggests a change toward a significantly more compact octameric conformation. The secondary structure of NSP2 showed a high fraction of β-sheet, with small changes induced by magnesium that were reversed in the presence of RNA. That NSP2 can exist in different conformations lends support to the previously proposed hypothesis (Taraporewala, Z., Chen, D., and Patton, J. T. (1999) *J. Virol.* 73, 9934–9943) of its function as a molecular motor involved in the packaging of viral mRNA.**

Rotavirus is a significant cause of disease in humans and animals. It is a member of the *Reoviridae*, and its genome consists of 11 segments of double-stranded RNA, which codes for six structural and six nonstructural proteins. The structural proteins include VP2, VP6, and VP7, which form the triple layered icosahedral virion capsid, the spike protein VP4, the RNA polymerase VP1, and the multifunctional capping enzyme VP3 (1) (for a review, see Ref. 2). Many studies have addressed the properties of the structural proteins, for example their spatial configuration in the virus particle using cryo-EM (3, 4), their antigenicity, and their role in viral entry, replication, or morphogenesis. Unfortunately, much less is known about the nonstructural proteins that are expressed and left behind in the infected cells.

Although it has been shown that these nonstructural proteins are not essential for replicase activity *in vitro* (5), they are important in several aspects of the replication cycle of the virus *in vivo*. Some of the more intensively studied nonstructural proteins include, for example, NSP4, which has a membrane-destabilizing activity and assists in the budding of newly synthesized inner capsid particles into the lumen of the endoplasmic reticulum (6, 7), where they acquire the outer coat protein VP7. NSP3 binds to the 3′-end of the viral mRNA and interacts with eukaryotic translation initiation factor eIF4G to enhance efficiency of translation (8). NSP2 and NSP5 interact to form viroplasms, large inclusions in the cytoplasm where core-like replication intermediates (core RIs)[1] are assembled and RNA replication takes place (2, 9, 10). As was shown in a study of a temperature-sensitive mutant, NSP2 is required for the formation of the viroplasm and is also essential in the synthesis of double-stranded RNA *in vivo* (11). However, little is known about the mechanism underlying this observation and the function of NSP2 on a molecular level.

NSP2 is a 35-kDa protein that forms homomultimers and interacts with the RNA polymerase VP1 (12, 17). Furthermore, NSP2 interacts with and induces hyperphosphorylation of NSP5 (13), which, in turn, interacts with NSP6 (14, 15), possibly forming a regulatory multiprotein complex. Both NSP2 and NSP5 possess a sequence-independent affinity for the binding of RNA (17) and are associated with the structural proteins VP1, VP2, and VP3 that form the core RIs that catalyze the synthesis of double-stranded RNA (16). It is thought that NSP2 and NSP5 have an active role in the packaging of RNA into cores (9). Recently, we have shown that NSP2 possesses an NTPase activity, which suggests an energy-dependent function for NSP2, possibly that of a molecular motor involved in the packaging of mRNA into core RIs (17).

In the present study, we have applied biophysical methods for the characterization of recombinant NSP2, with the goal to better understand the molecular structure of NSP2 in solution and the interaction with its ligands. In particular, we have studied the secondary structure, the oligomeric state, and the hydrodynamic shape of the protein in the presence of magnesium, nucleotide diphosphate and triphosphate, RNA, and DNA. As will be described below, we found that NPS2 self-assembles into relatively stable octamers, which can undergo conformational changes in the presence of magnesium and ADP. This may be of significance for understanding the function of NSP2.

## MATERIALS AND METHODS

*Protein and Oligonucleotides*—Recombinant NSP2 was prepared as described in detail in Ref. 17. In brief, a cDNA containing the NSP2 open reading frame of the simian rotavirus SA11 was cloned into the expression vector pQE60 (Qiagen). His-tagged rNSP2 was expressed in *Escherichia coli* M15[pREP4] cells (Qiagen) and purified using a $Ni^{2+}$-

* The costs of publication of this article were defrayed in part by the payment of page charges. This article must therefore be hereby marked "*advertisement*" in accordance with 18 U.S.C. Section 1734 solely to indicate this fact.

‖ To whom correspondence should be addressed: Laboratory of Infectious Diseases, National Institutes of Health, 7 Center Dr., MSC 0720, Rm. 117, Bethesda, MD 20892. Tel.: 301-496-3372; Fax: 301-496-8312; E-mail: jpatton@niaid.nih.gov.

[1] The abbreviations used are: RI, replication intermediate; DTT, dithiothreitol; ATPγS, adenosine 5′-*O*-(thiotriphosphate); r.m.s., root mean square.

nitrilotriacetic acid-agarose column. The protein was dialyzed overnight against 10 mM Tris-HCl, pH 7.2, 10 mM NaCl, 0.5 mM dithiothreitol (DTT), 0.5 mM EDTA (except where noted otherwise). The protein was obtained with a purity of >98%. The extinction coefficient and the partial specific volume of the protein were calculated from the amino acid composition using the program Sednterp (18). For the experiments with phosphorylated NSP2, the protocol described previously was applied (17), and the protein was incubated for 1 h at 37 °C in 5 mM $MgCl_2$ and 0.5 mM ATP. This was followed by dialysis against 10 mM Tris-HCl, pH 7.2, 10 mM NaCl, 0.5 mM DTT, and 0.5 mM EDTA.

For the study of nucleic acid binding of NSP2, a single-stranded 23-mer of RNA (RNA23) (5′-UGAAAACGGCGACUGAGGAUACC3′; Dharmacon Research) and single-stranded 23-mer of DNA (DNA23) (5′-TGAAAACGGCGACTGAGGATACC-3′; Life Technologies, Inc.) were used. The extinction coefficients of the oligonucleotides were determined spectrophotometrically.

*Sedimentation Equilibrium*—Sedimentation equilibrium studies were conducted in a Beckman Optima XL-A centrifuge, using an An50 Ti eight-hole rotor and absorbance optics. Double-sector charcoal-filled epon centerpieces were filled with 120–130 μl of sample at concentrations between 4 and 17 μM. Sedimentation equilibrium was attained at a rotor temperature of 4 °C and at rotor speeds of 8,000 rpm and 12,000 rpm. Absorbance profiles were acquired at wavelengths of 230, 250, and 280 nm, chosen according to the protein concentration. In the presence of oligonucleotide, ADP, or ATPγS, additional scans at 260 and 285 nm were taken. Data analysis was performed by global analysis of several data sets obtained at different loading concentrations and rotor speeds using the mathematical modeling software MLAB (Civilized Software, Silver Spring, MD). No thermodynamic nonidealities were observed, and least-squares fits were based on Boltzmann distributions of ideal species in the centrifugal field,

$$a_\lambda(r) = c(r_0)\varepsilon_\lambda d \exp\left[M(1-\bar{v}\rho)\frac{\omega^2(r^2-r_0^2)}{2RT}\right] + \delta \qquad \text{(Eq. 1)}$$

where $a_\lambda$ denotes the experimentally measured absorbance at a wavelength λ and at the distance $r$ from the center of rotation, $c$ and $\epsilon_\lambda$ the concentration and extinction coefficient of the protein, $d$ the optical path length of 1.2 cm, $M$ and $\bar{v}$ the protein molar mass and partial specific volume, $\rho$ the solvent density, $\omega$ the angular velocity of the rotor, $T$ the absolute temperature, $R$ the gas constant, $r_0$ an arbitrary reference radius, and δ a base-line absorbance (19), and their well known combination for models involving multiple species (20–22). Reported errors in the equilibrium analyses are calculated confidence intervals from $F$ statistics (23).

*Sedimentation Velocity*—Sedimentation velocity experiments were conducted in a Beckman Optima XL-I ultracentrifuge, using an An50 Ti eight-hole rotor and the interference optical detection system. Double-sector charcoal-filled epon centerpieces were filled with 350 μl of sample at concentrations between 1 and 10 μM. The rotor temperature was set between 20 and 24 °C, chosen to minimize temperature changes during a 1–2-h equilibration period of the rotor in the vacuum chamber prior to the start of the run. The rotor was then accelerated to 45,000 or 50,000 rpm at maximal rate, during which already visible sedimentation took place, as judged by the camera picture of the fringe profiles. Fringe displacement profiles were acquired in intervals of 30–40 s. Data were analyzed with the software SEDFIT, and errors reported are from replicate experiments.

The analysis of the sedimentation velocity profiles was performed by direct boundary modeling by solutions of the Lamm equation,

$$a(r,t) = \chi(r,t) + \varepsilon + \delta$$

$$\frac{d\chi}{dt} = \frac{1}{r}\frac{d}{dr}\left[rD\frac{d\chi}{dr} - s\omega^2r^2\chi\right] \qquad \text{(Eq. 2)}$$

where $a(r, t)$ denotes the experimentally measured absorbance, ε and δ the systematic and random signal offset, $s$ and $D$ the sedimentation and diffusion coefficients of the protein, and χ its concentration at position $r$ and time $t$ (24). This was combined with the algebraic calculation of systematic time-invariant and radial-invariant noise components ε (25). Because these systematic signals are arbitrary offsets introduced from the detection system, calculated systematic offsets can be subtracted from the raw data without introduction of bias if the degrees of freedom in the analysis are not reduced. Therefore, the final calculated best-fit offsets are subtracted from the raw data for presentation.

The Lamm equation solutions were calculated by using the finite element and moving frame of reference method described in Refs. 26–28, at a radial increment of ~0.001 cm. The finite element simulations were modified to include the consideration of the acceleration phase of the rotor. An average acceleration rate and duration was calculated based on the difference of the $\omega^2t$ and the $t$ entry of the data files, and the rotor speed-dependent matrix elements in the finite element algorithm were dynamically updated in intervals of 10 s for the calculated duration of the acceleration phase. In contrast to the previous strategy of calculating effective sedimentation times from the elapsed $\omega^2t$, which provides the correct boundary positions, the simulated acceleration phase additionally calculates the extent of diffusion during the acceleration phase and thereby improves the accuracy of the boundary shapes and leads to slightly improved quality of the fits. Using a model for multiple discrete species, the location of the meniscus was treated as a floating parameter and optimized in the nonlinear regression of the data. The resulting meniscus position was then used in the continuous size distribution analysis (see below).

To facilitate the analysis of systematic deviations in the fit, a two-dimensional bitmap representation of the residuals was calculated as described elsewhere.[2] In this picture, pixel rows represent the sequence of scans, and pixel columns represent different radial values. The brightness at each pixel is calculated by linearly mapping the values between −0.05 and +0.05 to grayscale values from 0 to 256. This transformation should result in a neutral gray picture without structure for a perfect fit, and any visible structure represents systematic deviations of the model from the data.

The sedimentation coefficient distributions were calculated by the $c(s)$ method by direct modeling with distributions of Lamm equation solutions,

$$a(r,t) = \int c_0(s)\chi(s, D(s), r, t)ds + \varepsilon + \delta \qquad \text{(Eq. 3)}$$

where $c_0(s)ds$ is the loading concentration of species with a sedimentation coefficient between $s$ and $s + ds$). Following the procedure outlined in detail in Ref. 30, the integral was solved by discretization into 250–300 $s$ values between 4 and 18 S (unless noted otherwise), and a value of 1.3 for the frictional ratio $f/f_0$ was used for estimating the average diffusional broadening of the sedimentation boundaries $D(s)$. Maximum entropy regularization was used to calculate the simplest size distribution within a confidence level of 0.68 of the best-fit distribution (30). While the use of the same frictional ratio for all species estimates the average degree of diffusion (corrected for the different macromolecular sizes via Stokes-Einstein relationship), a more refined calculation was performed once the ~12 S peak was identified as an octamer. The known molar mass of the oligomer was applied to all species in the sedimentation coefficient distribution within the range from 10 to 13.5 S, and diffusion coefficients were calculated directly by insertion of $s$ and $M$ into the Svedberg equation (19),

$$D = \frac{sRT}{M(1-\bar{v}\rho)} \qquad \text{(Eq. 4)}$$

For all species outside this predefined range of $s$ values, the approximation by using the frictional ratio was maintained. This method allows analyzing more rigorously the distribution of sedimentation coefficients for a macromolecule with known molar mass that can be present in different conformations, and its application leads to slightly sharper sedimentation coefficient distributions. To distinguish this distribution and indicate the use of a molar mass value, it will be referred to as $c_M(s)$ in the following.

*Dynamic Light Scattering*—Dynamic light scattering experiments were conducted with a Protein Solutions DynaPro 99 instrument with DynaPro-MSTC200 microsampler (Protein Solutions, Charlottesville, VA). Protein samples were drawn from the solution column after equilibrium sedimentation after the ultracentrifuge was stopped, and the cells were taken from the rotor with minimal convection. Although it is difficult to control the protein concentration in this way, this procedure is adequate for species analysis, and because of the persistent gradient close to equilibrium (31), it very effectively eliminates signal contributions from particles outside the size range of interest. A 20-μl sample was inserted in the 90° light scattering cuvette with the temperature control set to 20 °C. The autocorrelation coefficients were exported for analysis with the software SEDFIT, adapted for dynamic light scattering analysis by replacing the single species Lamm equation solutions by

[2] P. Schuck, D. Burkwall, W. Newcomb, D. Schubert, and J. Brown, submitted for publication.

the intensity correlation function,

$$g^{(2)}(\tau) = \exp[-2Dq^2\tau] \quad \text{(Eq. 5)}$$

where $\tau$ represents the decay time and $q = (4\pi n/\lambda)\sin(\Theta/2)$, with the solvent refractive index $n$, the wavelength of the incident light $\lambda$, and the scattering angle $\Theta$ (32). The size distribution analysis was performed analogous to the sedimentation coefficient distribution analysis, by replacing the Lamm equation solutions in the kernel by autocorrelation functions of the form in Equation 5.

*Circular Dichroism*—CD spectra of NSP2 and its complexes with ADP, RNA, and DNA were measured in a Jasco J-715 spectropolarimeter at 25 °C, using 1-mm path length quartz cuvettes. Control spectra were also measured on ADP, RNA, and DNA alone at the same concentrations, and the spectrum of the protein in the complexes was calculated as the difference between each sample and its control. Protein concentrations were 130–150 $\mu$g/ml. Four scans were made between 190 and 320 nm, at a speed of 50 nm/min, and with a time constant of 1 s. The measured ellipticities (*mdeg*) were converted into the mean residue ellipticity $\theta$ as follows,

$$\Theta = \frac{mdeg \times 10 \times MRW}{l \times c \times 100} \quad \text{(Eq. 6)}$$

where *MRW* is the mean residue weight (115.9), $l$ is the path length in cm, and $c$ is the protein concentration in mg/ml. Secondary structure was estimated from averaged spectra using the CONTIN program (33), and reported errors are from the variation of results for fits of a quality close to that of the best fit.

## RESULTS

*NSP2 Forms Octamers in Solution*—To characterize the state of association of NSP2, we have performed sedimentation equilibrium, sedimentation velocity, and dynamic light scattering experiments. Fig. 1 shows results from the hydrodynamic measurements. The sedimentation velocity profiles can be fit very well with a single species Lamm equation model with an $s$ value of $s_{20} = 11.96 \pm 0.1$ S. The analysis of the boundary spreading of the data shown in Fig. 1*A* gives a molar mass of 301 kDa, which is virtually identical to the molar mass of an octameric NSP2 of 301.4 kDa calculated from the amino acid composition. However, the error associated with this estimate from replicate experiments was observed to be approximately ±10–20 kDa. Therefore, direct measurements of the diffusion coefficients were performed separately by dynamic light scattering (Fig. 1*D*). The autocorrelation data were well described by a single component with $D_{20} = 3.63 \times 10^{-7}$ cm$^2$/s (with very minor impurities visible outside the size range of the protein). This value for $D$ is consistent with the boundary spreading of the sedimentation velocity data, as indicated by the excellent fit to the Lamm equation model using the predetermined $D$ (Fig. 1, *B* and *C*) with a root mean square (r.m.s.) deviation in the order of the instrument noise, and only minor systematic deviation visible in the residuals bitmap. Taking the values of $s$ and $D$ together, a molar mass estimate of 312 kDa is obtained. This strongly suggests that NSP2 is octameric in solution.

An independent confirmation of this result was obtained from sedimentation equilibrium experiments. As shown in Fig. 2, the sedimentation equilibrium distributions are well described at several loading concentrations and rotor speeds by a model for a single octameric species. When the molar mass is treated as an unknown parameter in the global analysis, a value corresponding to 7.8 ± 0.2 subunits is obtained. From the sedimentation equilibrium data alone, it cannot be ruled out that there might be significant populations of both heptamers and nonamers. However, the fact that the boundary spreading in sedimentation velocity experiments is consistent with that of a single octameric species strongly indicates the absence of heterogeneity of NSP2 and suggests that octamer formation is a highly specific process.

Sedimentation velocity experiments with phosphorylated NSP2 led to results indistinguishable from those of nonphosphorylated protein (data not shown). We also performed sedimentation velocity and equilibrium experiments with (nonphosphorylated) NSP2 in solutions of pH 5.2 and pH 9.2 and in varying concentrations of NaCl (0–100 mM). These experiments also led to virtually identical results (data not shown), indicating a high stability of the oligomer. Furthermore, consistent with the apparent absence of a slower sedimentation boundary in Fig. 1*A*, the fit to the sedimentation velocity data cannot be improved by allowing for a smaller species in the model, which indicates that the free NSP2 monomer concentration is below the sensitivity of the interference optical systems, which corresponds to concentrations of <0.1 $\mu$M.

After identifying the oligomeric state of NSP2 as an octamer, the sedimentation coefficient of $s_{20}$ of 11.96 S can be used to

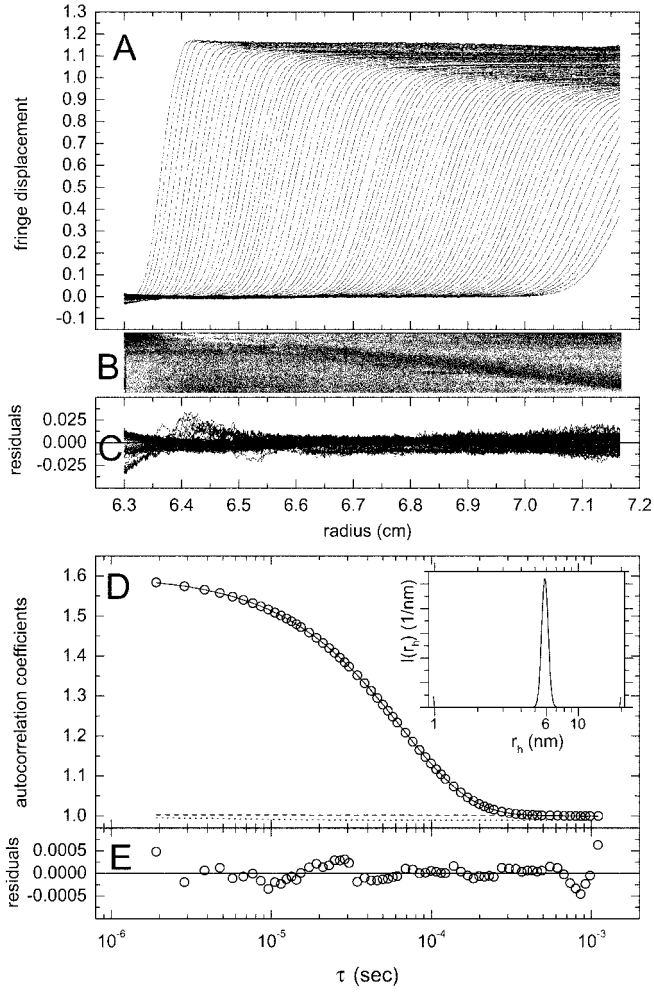


FIG. 1. **Hydrodynamic analysis indicates that NSP2 forms an octameric species.** *A*, sedimentation velocity data of 9.7 $\mu$M NSP2 in 10 mM Tris-HCl, pH. 7.2, 10 mM NaCl, 0.5 mM DTT, 0.5 mM EDTA, sedimenting at 50,000 rpm, 22 °C. *B* and *C*, bitmap and overlay representation of the residuals from a single-species model with $D_{20} = 3.81 \times 10^{-7}$ cm$^2$/s (predetermined from dynamic light scattering) and with $s_{20} = 11.97$ S, which leads to a r.m.s. deviation of 0.0059 fringes. *D*, autocorrelation coefficients from a dynamic light scattering experiment (*circles*) and best-fit autocorrelation function (*solid line*) based on a model for the species $D_{20} = 3.81 \times 10^{-7}$ cm$^2$/s, in the presence of signal contributions of two species with $D_{20} = 27.1 \times 10^{-7}$ cm$^2$/s (1.2% total signal contribution) (*dotted line*) and $D_{20} = 0.057 \times 10^{-7}$ cm$^2$/s (2.1%) (*dashed line*). These contaminating species are not visible in the sedimentation velocity profiles. The *inset* shows the distribution of hydrodynamic radii (in nm), with a peak at 5.8 nm. *E*, residuals of the fit, which has a r.m.s. deviation of $1.8 \times 10^{-4}$. Assuming a partial specific volume of 0.74 ml/g, a molar mass of 312 kDa is obtained when combining the values of $s$ and $D$.

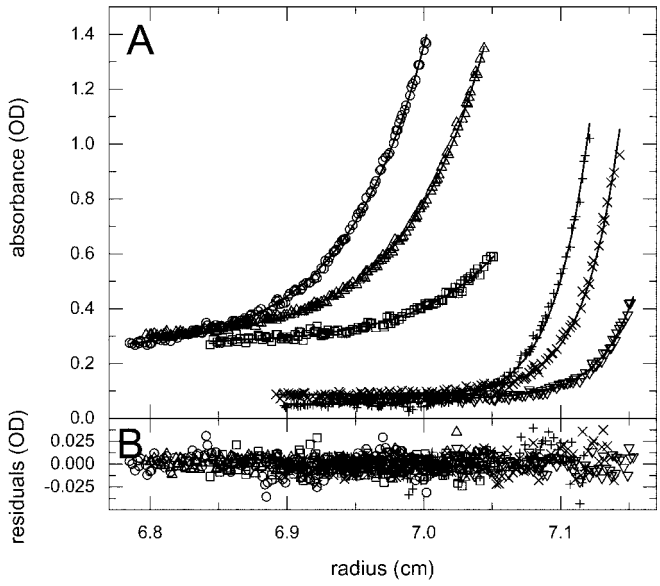


FIG. 2. **NSP2 in sedimentation equilibrium can also be modeled as an octameric species.** NSP2 in 10 mM Tris-HCl, pH 7.2, 100 mM NaCl, 0.5 mM DTT, 0.5 mM EDTA in sedimentation equilibrium at 4 °C. *A*, experimental absorbance profiles at 280 nm at a loading concentration of 17 $\mu$M (*circles*), 8 $\mu$M (*triangles*), and 4 $\mu$M (*squares*) at 8,000 rpm (all offset by 0.2 OD and −0.1 cm), and 17 $\mu$M (+), 8 $\mu$M (×), and 4 $\mu$M (*inverted triangles*) at 12,000 rpm. *Solid lines* are the best-fit single species distribution with a molar mass of 301.4 kDa. *B*, residuals of the fit, which lead to an r.m.s. deviation of 0.011 OD.

calculate a frictional ratio of 1.30 and a Stokes radius of 5.8 nm. In terms of gross hydrodynamic shape, with an estimated hydration ratio of 0.383 *g/g* calculated from the amino acid composition (18, 34) these values would correspond to an equivalent prolate ellipsoid with major and minor axis of 22.5 × 6.9 nm or to an equivalent oblate ellipsoid with dimensions 15.4 × 4.5 nm. Qualitatively similar values for the dimensions of the equivalent ellipsoids are obtained with a lower estimate for the hydration (Table I).

*NSP2 Octamers Dissociate in the Presence of Magnesium*—Since it was shown recently that NSP2 has an NTPase activity, for which the presence of magnesium is an essential cofactor, with optimal concentrations between 1 and 5 mM $MgCl_2$ (17), we next studied the protein in 5 mM $MgCl_2$. It can be seen from Fig. 3 that under these conditions NSP2 exists in a heterogeneous mixture of species, including populations that sediment significantly slower than the octamer. This effect disappeared when overnight dialysis in buffer without $MgCl_2$ followed the incubation with magnesium, which indicates the reversibility of the observed magnesium effect. As is described below, this change in the oligomeric state by magnesium is also accompanied by small changes in secondary structure.

To unravel the distribution of species, the sedimentation coefficient distribution was determined. The commonly used approach for a model-free analysis is an apparent sedimentation coefficient distribution $g^*(s)$, which operates in the approximation of $D = 0$ (no diffusion). A much more realistic treatment for diffusion has recently been developed, where an approximate average frictional ratio is used to estimate the diffusion coefficients $D(s)$ as a function of the sedimentation coefficient (30), and initial applications have demonstrated the high resolution achieved (35).[2] The resulting distributions $c(s)$ are not diffusionally broadened, and the residual width of the peaks obtained for discrete protein species is dependent on the correctness of the shape assumption and (due to the maximum entropy regularization employed) on the signal-to-noise ratio of the data. We have used this method in the present study with

TABLE I
*Estimated dimensions of equivalent hydrodynamic ellipsoids for NSP2*

| Oligomer | $s_{20}$ | Stokes radius[a] | Prolate ellipsoid[b] | Oblate ellipsoid[b] |
|---|---|---|---|---|
| | *S* | *nm* | *nm* × *nm* | *nm* × *nm* |
| Octamer | 11.96 | 5.8 | 22.5 × 6.9 (25.3 × 6.0) | 15.4 × 4.5 (16.0 × 3.5) |
| Octamer with Magnesium | 11.80 | 5.9 | 23.5 × 6.8 (26.3 × 5.9) | 15.8 × 4.3 (16.3 × 3.4) |
| Octamer with ADP | 12.61 | 5.5 | 18.4 × 7.6 (21.6 × 6.4) | 13.8 × 5.6 (14.7 × 4.2) |
| Tetramer with magnesium | 6.44 | 5.4 | 27.2 × 4.4 (29.2 × 3.9) | 15.5 × 2.2 (15.7 × 1.9) |

[a] Calculated from molar mass and sedimentation coefficient.
[b] 2-fold major and minor axis, calculated under the assumption of a hydration of 0.383 g/g, as predicted from the amino acid composition (18,34). For comparison, values assuming a lower hydration of 0.2 g/g are given in parenthesis.

the estimate 1.3 for $f/f_0$ of all species, using the property of $c(s)$ that it is not very sensitive to this value and assuming that the frictional ratio of the octameric NSP2 may be a reasonable approximation for the other unknown species. The resulting $c(s)$ distribution obtained from the data presented in Fig. 3*A* shows two main peaks at 6.4 S (24%) and 11.9 S (57%) as well as very small populations at 3.5 S (2%), between 8 and 10 S (7.6%), and at 14.5 S (3.1%).

A discrete Lamm equation analysis was also performed to analyze the boundary spreading from the ~12 S species. This resulted in a molar mass estimate of 306 ± 10 kDa, suggesting that this species is still octameric. To further improve the size distribution analysis by utilizing this knowledge of the 12 S species being octameric with a theoretical molar mass of 301 kDa, we have modified the $c(s)$ method such that the diffusion coefficients of the species between 10 and 13 S are calculated by the Svedberg equation. This combines the "model-free" analysis of the sedimentation coefficient distribution with the assignment of the ~12 S peak as the octamer, and instead of assuming shape similarity, it constitutes a model more appropriate for protein complexes with possible conformational changes (termed $C_M(s)$). The results are shown in Fig. 3*D*, clearly reflecting the multimodal boundary shape, with populations of protein at ~3.5, 6.44, ~9, 11.90, and ~15 S.

In both the continuous $c(s)$ and the discrete Lamm equation analysis, it is apparent that the sedimentation coefficient of the octamer appears at a slightly lower value of 11.80 S. Although this difference in the octameric sedimentation coefficient induced by magnesium is very small, it was reproducible and significant when results from the same protein preparation and from the same velocity run were compared. One possible explanation of this smaller *s* value could be a shift in the apparent peak *s* value due to the chemical reaction of the protein coupled to the sedimentation. However, dissociation of the octamer was slow compared with the sedimentation. When interpreted in the context of hydrodynamic shape, this small increase in the hydrodynamic friction would correspond to a slightly more asymmetric shape of the octamer (Table I).

The identification of the nature of the second most abundant species at 6.4 S is more difficult, although this *s* value can theoretically only be assumed by oligomers larger than the dimer. Sedimentation equilibrium profiles and dynamic light scattering data were acquired (data not shown), but they lead to ill conditioned analyses. From dynamic light scattering, the distribution of Stokes radii showed a single peak at 5.9 nm. In sedimentation equilibrium, the weight-average molar mass corresponded to 6.9 subunits, and a two-component model of the sedimentation equilibrium with an octameric species and an unknown oligomer resulted in the average subunit number

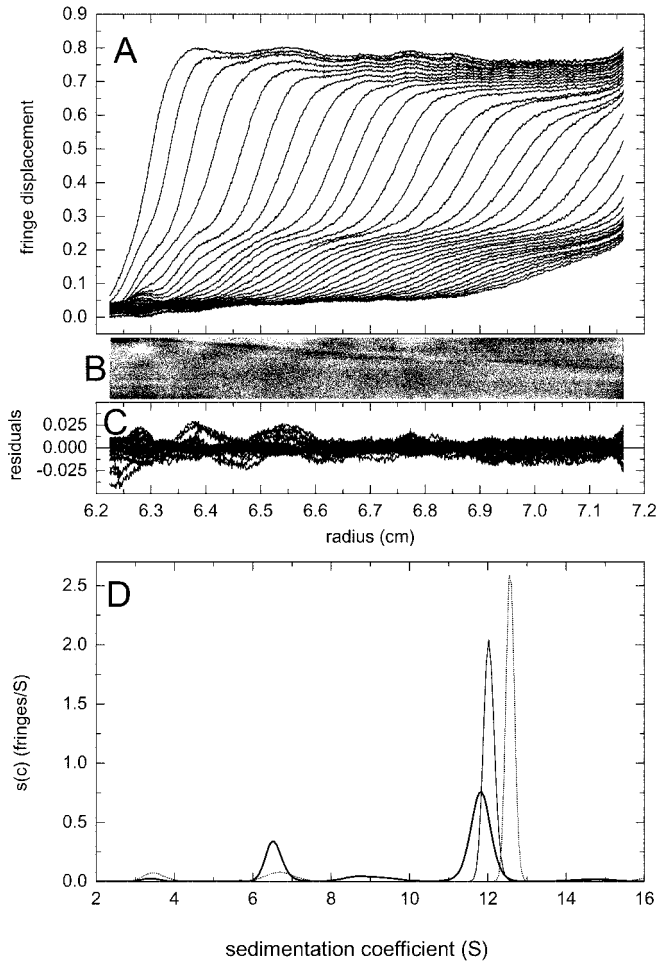


FIG. 3. **NSP2 exhibits a mixture of fast and slow sedimenting species in the presence of Mg.** *A*, sedimentation velocity data of 6.6 $\mu$M NSP2 in 10 mM Tris-HCl, pH 7.2, 10 mM NaCl, 5 mM $MgCl_2$, 0.5 mM DTT, 0.5 mM EDTA, sedimenting at 50,000 rpm, 20 °C. For clarity, every fifth scan is shown. *B* and *C*, bitmap (all scans) and overlay representation (every fifth scan) of the residuals from the continuous $c_M(s)$ model when constraining the molar mass of all species between 10 and 13 S to 301 kDa, as a model for the sedimentation coefficient distribution of octameric NSP2 with different conformational states. The boundary spreading of all other species (slower than 10 S and faster than 13 S) was estimated via a frictional ratio of 1.3. The r.m.s. deviation is 0.0062 fringes. The resulting $c_M(s)$ distribution is shown in *D* (*solid line*). Also shown in *D* is the corresponding $c_M(s)$. distribution of the same NSP2 sample in 5 mM Mg after the addition of 1 mM ADP (*dotted line*), and for reference the $c_M(s)$ distribution in the absence of Mg and ADP (*dashed line*).

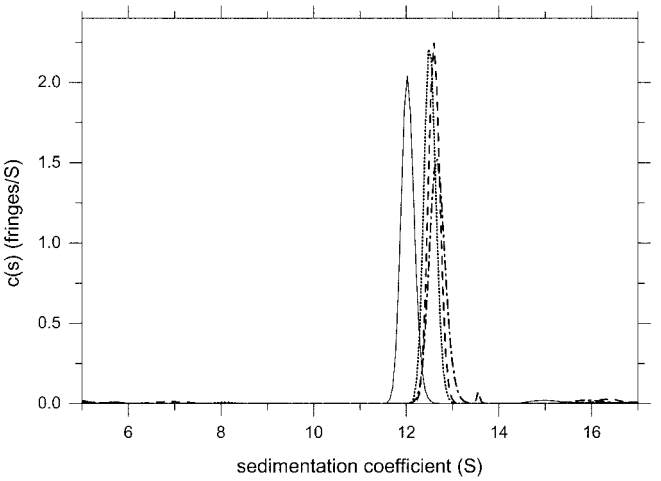


FIG. 4. **ADP and ATP$\gamma$S induce conformational change in NSP2.** Sedimentation coefficient distributions $c_M(s)$ from the conformational change model for species between 10 and 13.5 S. NSP2 in 10 mM Tris-HCl, pH 7.2, 10 mM NaCl, 0.5 mM DTT, 0.5 mM EDTA is shown for reference (*solid line*) and after the addition of 1 mM ADP (*dashed line*), 1 mM ADP plus 5 mM $MgCl_2$ (*dashed and dotted line*), or 1 mM ATP$\gamma$S plus 5 mM $MgCl_2$ (*dotted line*).

of 5.5 for the smaller species, although good fits with a tetramer/octamer model could be obtained. This suggests that the second major peak in the sedimentation coefficient distribution may be a tetramer, with the species between 8 and 10 S being intermediates. Results from the interpretation of the gross hydrodynamic shapes are summarized in Table I.

*ADP and ATP$\gamma$S Bind to Octameric NSP2 and Increase the Sedimentation Coefficient*—As the next step, we examined effects of nucleotide diphosphate and a triphosphate analogue on the conformation of NSP2. Fig. 4 shows the sedimentation coefficient distributions $c_M(s)$ of NSP2 in the presence of 1 mM ADP obtained from velocity centrifugation. It is clearly visible that NSP2 is sedimenting faster, with a sedimentation coefficient of $s_{20}$ = 12.61 S. To rule out the possibility that larger oligomers may have formed, we calculated the apparent molar mass from boundary spreading to be 296–306 kDa. The analysis of the autocorrelation coefficients from dynamic light scattering in the presence of ADP leads to a $D_{20}$ value of $3.71 \times 10^{-7}$ $cm^2/s$ (data not shown), which, taken together with the sedimentation coefficient of 12.61 S, corresponds to a molar mass of 318 kDa. Therefore, within experimental uncertainty, this is consistent with the molar mass of the NSP2 octamer.

This indicates that the oligomeric state of NSP2 is not affected by the binding of ADP. Unfortunately, we were unable to unambiguously clarify the origin of the increased sedimentation coefficient. However, the sedimentation coefficient of NSP2 is increased by 5%, which is a significantly larger increase than one would expect on the basis of the additional mass of eight nucleotides (assuming one binding site per protomer; to account for the increased sedimentation rate through the additional mass of bound nucleotides alone, this would require >30 nucleotides if the frictional coefficient of the complex would not change, or >45 nucleotides with the usual ⅔ power rule). Instead, taken together with the observed increase in the diffusion coefficient and the corresponding decrease of the hydrodynamic radius, the shift in the sedimentation coefficient suggests a conformational change toward a more compact hydrodynamic shape (Table I). As is visible in Fig. 4, a similar shift in the sedimentation coefficient by 0.65 S is obtained when 1 mM ADP or ATP$\gamma$S is added in the presence of 5 mM $MgCl_2$. Furthermore, a similar increase of the sedimentation coefficient was observed for phosphorylated NSP2 (data not shown).

To study in more detail the nature of this faster sedimenting protein-nucleotide complex, we performed sedimentation velocity experiments in the presence of 50 mM NaCl (so as to diminish the potential electrostatic interactions of the nucleic acid binding sites of the basic protein with the nucleotides) and with different nucleotide concentrations. First, at an ADP concentration of 50 $\mu$M, we applied multidetection to observe simultaneously the sedimentable absorbance at 260 and 280 nm, as well as the fringe shift data for the total protein distribution (data not shown). From the ratio of 260- to 280-nm absorbance, we found that at this concentration ~0.3 nucleotides are bound per protein protomer. Surprisingly, no shift in the sedimentation coefficient was observed in comparison with a control sample without nucleotides. When the ADP concentration was increased, no shift in the sedimentation coefficient was observed below 0.4 mM, while above this concentration the sedimentation coefficients were consistently higher by 0.6–0.7 S.

No significant difference in the *s* value between 1 and 2 mM ADP was observed. (Unfortunately, due to the high extinction of the nucleotides, absorbance detection for the measurement of protein/nucleotide ratio is not possible at nucleotide concentration higher than ~50 μM.) Although the limited precision of the small changes in the *s* values does not permit the interpretation of an isotherm $s(c)$, this steep concentration dependence in the range of 0.5 mM would be consistent with a cooperative transition of the octamer conformation. In experiments with the nonhydrolyzable analogue ATPγS, we found already a significant $\Delta s$ at concentrations of 0.1 mM, suggesting a higher affinity of this nucleotide.

An additional aspect of nucleotide binding can be observed in the absence of a slower sedimenting component in Fig. 4, which shows that nucleotide binding prohibits the $MgCl_2$-induced dissociation of NSP2. To see if binding of ADP can lead to reassembly of NSP2 that was already dissociated by 5 mM $MgCl_2$, we performed a sequential sedimentation velocity experiment. After measuring the sedimentation profiles shown in Fig. 3*A*, we mixed the solution in the ultracentrifuge cell to resuspend the sedimented protein. (In control experiments, we observed that mixing the solution column and restarting a second velocity experiment did not change the sedimentation parameters, and full resuspension of the material was achieved.) We then added 1 mM ADP to the solution and incubated for 3 h, before starting a new velocity run. The resulting sedimentation coefficient distribution is shown by the *dotted line* in Fig. 3*D*. After the addition of ADP, the population was shifted from the dissociated state back to an octamer in the more compact form, indicating that the $MgCl_2$-induced dissociation is reversed by binding of ADP. However, no complete reversibility was observed, which may indicate a slow kinetic process of reassembly.

*NSP2 Octamer Binds RNA and DNA*—It has been shown previously that NSP2 binds both RNA and DNA with high affinity, which may be central to its function (17).[3] Therefore, we were interested in the effects of nucleic acid binding to the protein. For the present study, we have chosen short oligonucleotides (23-mers) to simplify the protein-RNA/DNA interaction and to avoid the possible cooperative binding of more than one functional unit of NSP2 to a nucleic acid strand, forming larger complexes such as those observed previously by electrophoretic mobility shift assays (17).

First, we wanted to demonstrate that RNA23 binds NSP2 under our experimental conditions. Therefore, we performed sedimentation equilibrium experiments, with absorbance scans acquired at the absorbance maxima of both the protein and the nucleic acid (Fig. 5). The equilibrium distribution could be well modeled with a single species of 301 kDa. (It can be expected that the buoyant molar mass of the oligonucleotides is negligible compared with the octameric protein.) Since the sedimenting absorbance at 260 nm is significantly larger than would be expected based on the protein extinction at this wavelength (*dashed line* in Fig. 5*A*), it is apparent that the RNA23 is bound to the NSP2 octamer. The quantitative analysis of the increased absorbance signal at 260 nm leads to a molar ratio of 2.0 ± 0.4 RNA23 molecules per NSP2 octamer. Similar results were obtained for the binding of DNA23.

As an independent measurement of the oligomeric state of NSP2 when bound to nucleic acid, we performed sedimentation velocity experiments (Fig. 6). The sedimentation coefficient distribution of the NSP2-nucleic acid complex shows a peak at $s_{20}$ = 12.11 ± 0.03 S (Fig. 6*D*) (12.06 ± 0.06 S for DNA23), which is consistent with the value of $s_{20}$ = 11.96 S in the absence of oligonucleotides, considering the small increase in mass. To study the effect of other ligands, we performed sedimentation velocity experiments in the presence of ADP or $MgCl_2$. When 1 mM ADP was present, the protein-RNA complex sedimented at a slightly higher rate of 12.38 (0.04) S (12.35 S for the protein-DNA23 complex). In the presence of $MgCl_2$, a value of 12.04 S was measured, accompanied by some dissociation of the octamer (Fig. 6*D*). These shifts in the sedimentation coefficient distributions are consistent with the effects of nucleotides and magnesium on the protein alone (Fig. 3*D*). However, the magnesium-induced dissociation seemed to be less in the protein/RNA mixture. Additionally, a sequential sedimentation velocity experiment performed with 9.7 μM NSP2 and 5 mM $MgCl_2$, followed by resuspension of the solution, incubation with 1.5 μM RNA23, and a repeat sedimentation velocity experiment indicated a 15% increase in the population of octamer after the addition of RNA (data not shown). In a separate sedimentation velocity experiment with DNA23 in 5 mM $MgCl_2$ after longer incubation, no dissociation was observed, and as described in the following, the secondary structure changes induced by magnesium are absent in the presence of RNA or DNA.

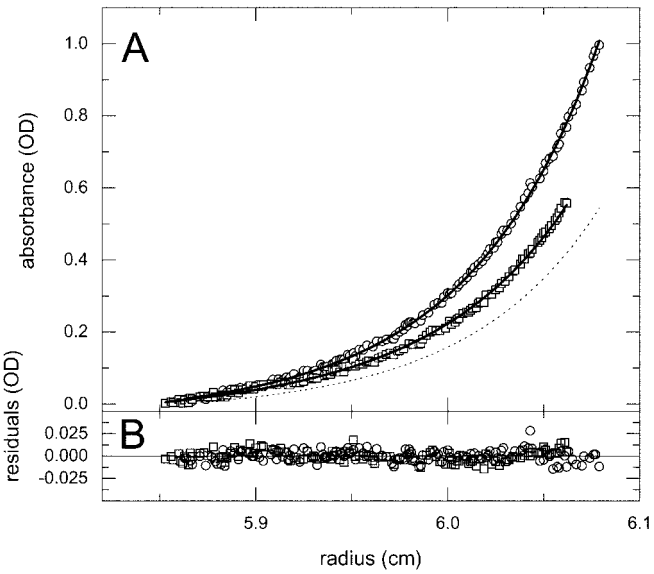


FIG. 5. **RNA binds to octameric NSP2.** *A*, absorbance scans of 9.7 μM NSP2 in sedimentation equilibrium with 1.5 μM RNA23 are shown at wavelengths of 280 nm (*circles*) and 260 nm (*squares*). As calculated from the absorbance ratio, two RNA23 molecules bind per NSP2 octamer. *Solid lines* are calculated best-fit distribution for octameric NSP2. For comparison, the *dashed line* shows the signal at 260 nm that would be expected for the protein alone. Experimental conditions were as follows: 10 mM Tris-HCl, pH 7.2, 100 mM NaCl, 0.5 mM DTT, 0.5 mM EDTA in sedimentation equilibrium at 8,000 rpm and at 4 °C. *B*, residuals of the fit.

*Circular Dichroism Studies of the Secondary Structure of NSP2*—Fig. 7*A* shows the CD spectrum of NSP2, typical of an α/β protein. Analysis with the CONTIN program gave a best fit with estimates of 24% α-helix and 45% β-sheet. The addition of 5 mM $MgCl_2$ seemed to be accompanied by a small change in secondary structure (best fit 32% α-helix, 35% β-sheet), apparent from Fig. 7*A* in the decreased ellipticity at 210 nm. This indicates that the observed dissociation is accompanied by or the result of changes in the secondary protein structure. After incubation of the protein-magnesium complex for 24 h, magnesium-induced change seemed to be reversed with 1.5 μM RNA23 or 1.5 μM DNA23 (Fig. 7*B*). This supports the reversibility of the magnesium effect on the protein by binding of oligonucleotides as observed by sedimentation velocity (above). Because their spectra were of such low intensities, it was im-

[3] Z. Taraporewala and J. T. Patton, (2001) *J. Virol.*, in press.

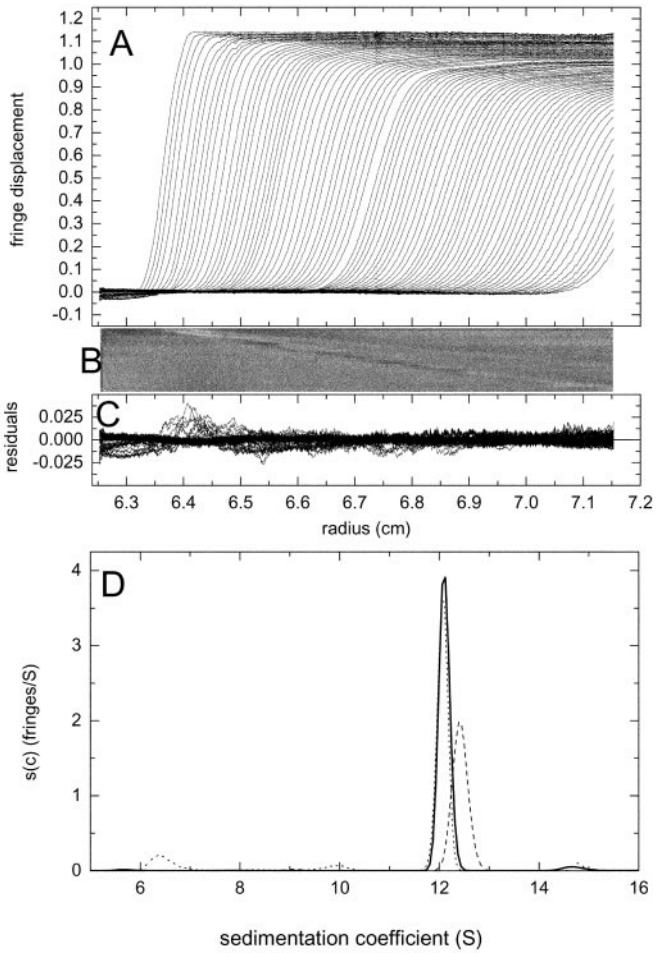


FIG. 6. **NSP2 is octameric in the presence of RNA.** *A*, sedimentation velocity data of 9.7 $\mu$M NSP2 and 1.5 $\mu$M RNA23 in 10 mM Tris-HCl, pH 7.2, 10 mM NaCl, 0.5 mM DTT, 0.5 mM EDTA, sedimenting at 50,000 rpm, 22 °C. *B* and *C*, bitmap and overlay representation of the residuals from the continuous *c*(*s*) model. The r.m.s. deviation is 0.0044 fringes. The resulting *c*(*s*) distribution is shown in *D* (*solid line*). For comparison, *D* also shows the *c*(*s*) distribution obtained in the presence of 1 mM ADP (*dashed line*) and 5 mM $MgCl_2$ (*dotted line*).

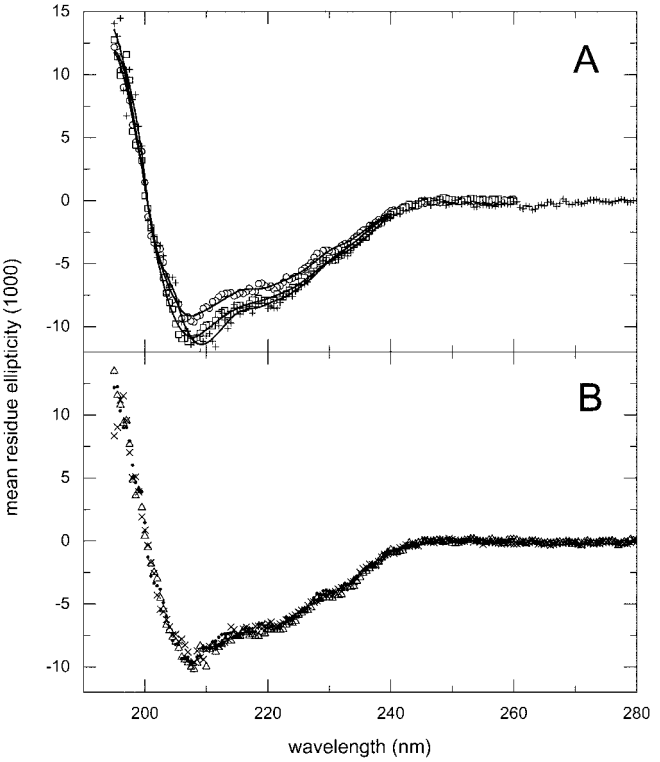


FIG. 7. **CD spectra of NSP2.** *A*, CD spectrum of NSP2 is shown (*circles*) with best fit corresponding to 24% $\alpha$-helix (24–28%) and 45% $\beta$-sheet (29–50%) (*solid line*). Also shown are CD data in the presence of 5 mM $MgCl_2$ (*squares*) with a best fit of 32% $\alpha$-helix (30–36%), 35% $\beta$-sheet (27–36%) (*solid line*), and in the presence of 5 mM $MgCl_2$ and 1 mM ADP (+) with a best fit of 23% $\alpha$-helix (14–32%), 55% $\beta$-sheet (26–58%) (*solid line*). *B* shows the spectra of NSP2 in the presence of 1.5 $\mu$M RNA23 (×) (best fit leads to 24% $\alpha$-helix (23–29%), 35% $\beta$-sheet (28–41%)) or 1.5 $\mu$M DNA23 (△) (24% $\alpha$-helix (24–28%), 22% $\beta$-sheet (22–41%)). As a reference, the CD spectrum of NSP2 is also shown again (*solid circles*).

possible to detect any conformational changes induced in the nucleic acids after binding to the protein. Interestingly, the addition of 1 mM ADP did not appear to restore protein secondary structure to its state in the absence of magnesium and nucleotide (Fig. 7*A*, best fit 23% $\alpha$-helix, 55% $\beta$-sheet), suggesting that the conformational change that leads to a more compact octamer is also accompanied by small changes in the secondary structure.

## DISCUSSION

In the present paper, we have applied hydrodynamic and thermodynamic techniques and CD spectroscopy to the study of structural aspects of NSP2 of rotavirus in solution, with the goal to better understand the function of NSP2 in the life cycle of the virus. It was shown previously that NSP2 assembles into multimers (12, 17), which were also detected in infected cells (12). Our results indicate that these multimers are highly stable octamers, formed by very specific and strong self-assembly, and that they are the oligomeric state relevant for RNA binding of the protein as well as NTPase activity. Furthermore, our data show that NSP2 can undergo conformational changes that are controlled by its ligands. Several structural and functional consequences will be discussed in the following.

From circular dichroism, we found that the secondary structure of the protein contains a high amount of $\beta$-sheet. This correlates well with the secondary structure found for single-stranded DNA-binding proteins of several other organisms (37–40). With respect to the tertiary and quaternary structure, as has been pointed out previously, single-stranded DNA-binding proteins exhibit a great variety of oligomeric states in different species (37), and they also differ in the mode of DNA binding. While some partial similarities of NSP2 with other single-stranded DNA-binding proteins can be observed, it may be that NSP2 adopts a novel quaternary structure.

It has been demonstrated that the helicase Dmc1, a eukaryotic homologue of the *E. coli* RecA, forms an octameric ring with a central channel for binding DNA (41). The Dmc1 octamer appeared in electron micrographs as a symmetrical side-by-side arrangement of eight monomers, similar to the hexameric ring-structure of other helicases (42). Despite the same number of subunits of Dmc1 and NSP2 involved in polynucleotide binding, the ability of the NSP2 to dissociate in relative distinct tetrameric subunits does not seem to support a strong structural relationship between these proteins. (Interestingly, initial sedimentation velocity experiments with a protein related to NSP2, the NS2 protein from bluetongue virus, could be modeled on the basis of a rapidly reversible monomer-tetramer-octamer self-association equilibrium.)[4] SSB proteins from *E. coli* and several other species have been found to be tetrameric (43–46), with DNA wrapped around the protein complex (44, 47). EcoSSB can cooperatively multimerize to

[4] P. Schuck, Z. Taraporewala, P. McPhie, and J. T. Patton, unpublished data.

higher oligomers when bound to the nucleic acid, and it has been proposed that this includes the formation of octamers through the dimerization of tetramers (48); similar octameric forms were also suggested for the vaccinia virus I3L gene product (49). However, generally little sequence similarity of EcoSSB and related proteins with the single-stranded DNA-binding proteins of animal viruses are found (50), and it is not clear if NSP2 and EcoSSB share more structural motifs than a high fraction of $\beta$-sheet. Supporting this view are preliminary pictures from cryo-EM reconstructions,[5] which show a barrel-shaped particle, for which one could speculate that the central cavity in the NSP2 may be the binding site for mRNA (36), either accommodating a loop of mRNA or with NSP2 threaded on the nucleic acid strand.

From the data described in the present paper, we found that the octamer has a Stokes radius of 5.8 nm and frictional ratio of 1.3, which indicates that it is spatially not very compact. Binding of magnesium is accompanied by small conformational changes in the secondary structure and by significantly weaker self-association of the protein, which allows additional insight into the structure of the protein. Our data suggest that in the presence of magnesium the octamer may adopt a slightly more "loose" conformation and partially dissociates, with the main smaller species probably being a tetramer. When using the gross hydrodynamic models of equivalent ellipsoids, in the prolate model the tetramer would appear more extended than the octamer, while in the oblate model it would appear to be approximately half the thickness of the octamer. Because a possible mechanism of octamer formation would consist of the dimerization of two tetramers, it is noteworthy that the oblate model would suggest an arrangement with two tetramers stacked on top of each other. Unfortunately, because of the poor ability of hydrodynamic modeling to predict precise molecular shapes, the clarification of the spatial structure has to await the results from methods with higher resolution.

A second type of conformational change of NSP2 was observed when nucleotide diphosphates or triphosphates were bound. Under these conditions, a small but significant increase of the rate of sedimentation was observed, corresponding to a more compact octameric conformation with a frictional ratio of 1.23. One alternative explanation for this may be the binding of a large number of nucleotides to the protein, possibly through electrostatic interactions. However, our studies with buffers of different ionic strength and at different nucleotide concentrations make this appear unlikely. Furthermore, the steep concentration dependence of the shift in sedimentation rate rather suggests the hypothesis of an allosteric, cooperative transition in the octamer conformation. Interestingly, nucleotides also seem to reverse the effect of magnesium to weaken the intersubunit interactions of the octamer. As judged by the oblate ellipsoid model, the total spatial amplitudes of the conformational changes corresponding to the increased sedimentation rate are 1.3 and 2 nm. Despite the lack of precise three-dimensional structures at the current stage, these changes are highly significant. Since we did not observe large effects of ADP or ATP$\gamma$S on the secondary structure, this shape change may involve rearrangement of protein domains.

The role of these conformational changes of NSP2 is not clear. Although, in principle, it could provide for an allosteric regulatory mechanism, the conformational changes may also have a more specific role as mechanical transducers. Because NSP2 associates with core RIs and cross-linking of infected cell-lysates showed it to interact with the RNA polymerase VP1 (12), it has been implicated in the packaging of mRNA into cores (9, 36). Based on the finding of NTPase activity of NSP2, it has recently been suggested that the protein may function as a molecular motor (17), possibly utilizing the energy obtained from hydrolysis for the transport of mRNA through the channels of core RIs. Since a molecular motor requires at least two distinct conformational states with mechanically different shapes, the changes of hydrodynamic shape from a loose to a more compact or tight conformation upon nucleotide binding is consistent with such a hypothesis. However, we have insufficient knowledge of how the reverse change from the compact to the more loose conformation would take place, and how this could be exploited for packaging. So far, only few findings seem to provide partial insights. Both ADP and ATP$\gamma$S bind NSP2 in the tighter conformation (Fig. 4), although ATP$\gamma$S may have a higher affinity. We did not find a difference in the hydrodynamic behavior as a result of phosphorylation, and it has been shown that phosphorylated NSP2 retains mRNA binding activity (17). In the absence of nucleotides, binding of mRNA occurs to the loose conformation. Clearly, a more detailed study of mRNA interaction with the protein under the different conditions is required (see below).

On the other hand, this mechanical NSP2 function could also require the interaction with other viral proteins, such as NSP5. NSP5 and NSP2 coimmunoprecipitate in the presence of RNA after UV cross-linking (29), and both proteins can be cross-linked with the RNA polymerase VP1 (13), suggesting that NSP5 also is a component of the multiprotein complex that possesses replicase activity (13, 29, 36). Also, NSP2 up-regulates the phosphorylation of NSP5 (13), possibly by transfer of the phosphate group obtained from the NTPase activity of NSP2 (17). The conformational changes of NSP2 observed here after binding of nucleotides seem to add an additional perspective of the NSP2-NSP5 interaction with regard to a possible role of NSP5 in assisting the conformational transitions in a multiprotein complex.

In the present study, we have focused on the oligomeric state of the NSP2 protein. Combining the findings from ultracentrifugation and CD spectroscopy that the octameric NSP2 binds RNA and that RNA binding stabilizes the octamer suggests that this is the functional unit for RNA binding. In a recent study, it was observed that NSP2 exhibits a nucleotide- and magnesium-independent strand displacement activity,[3] which could play a role in the unwinding of the mRNA template used for double-stranded RNA synthesis. Interestingly, this activity was inhibited in a concentration-dependent way by magnesium, which parallels our observation that magnesium causes partial dissociation of the NSP2 octamer into tetramers. Further studies will be required that investigate the stoichiometry of the protein-mRNA complexes, the possibility of cooperative binding of multiple NSP2 octamers to longer RNA strands (17), and the affinity of mRNA for NSP2 in the different conformations.

[5] H. Jayaram, Z. Taraporewala, J. T. Patton, and B. V. V. Prasad, unpublished data.

REFERENCES

1. Chen, D., Luongo, C. L., Nibert, M. L., and Patton, J. T. (1999) *Virology* **265,** 120–130
2. Estes, M. K. (1996) in *Fundamental Virology* (Fields, B. N., Knipe, D. M., and Howley, P. M., eds) pp. 731–761, Lippincott Williams & Wilkins, Philadelphia
3. Prasad, B. V., and Chiu, W. (1994) *Curr. Top. Microbiol. Immunol.* **185,** 9–29
4. Prasad, B. V., Burns, J. W., Marietta, E., Estes, M. K., and Chiu, W. (1990) *Nature* **343,** 476–479
5. Chen, D., Zeng, C. Q., Wentz, M. J., Gorziglia, M., Estes, M. K., and Ramig, R. F. (1994) *J. Virol.* **68,** 7030–7039
6. Tian, P., Ball, J. M., Zeng, C. Q., and Estes, M. K. (1996) *J. Virol.* **70,** 6973–6981
7. Tian, P., Ball, J. M., Zeng, C. Q., and Estes, M. K. (1996) *Arch. Virol. Suppl.* **12,** 69–77
8. Vende, P., Piron, M., Castagne, N., and Poncet, D. (2000) *J. Virol.* **74,** 7064–7071
9. Patton, J. T., and Spencer, E. (2000) *Virology* **277,** 217–225

10. Fabbretti, E., Afrikanova, I., Vascotto, F., and Burrone, O. R. (1999) *J. Gen. Virol.* **80,** 333–339
11. Chen, D., Gombold, J. L., and Ramig, R. F. (1990) *Virology* **178,** 143–151
12. Kattoura, M. D., Chen, X., and Patton, J. T. (1994) *Virology* **202,** 803–813
13. Afrikanova, I., Fabbretti, E., Miozzo, M. C., and Burrone, O. R. (1998) *J. Gen. Virol.* **79,** 2679–2686
14. Torres-Vega, M. A., Gonzalez, R. A., Duarte, M., Poncet, D., Lopez, S., and Arias, C. F. (2000) *J. Gen. Virol.* **81,** 821–830
15. Gonzalez, R. A., Torres-Vega, M. A., Lopez, S., and Arias, C. F. (1998) *Arch. Virol.* **143,** 981–996
16. Gallegos, C. O., and Patton, J. T. (1989) *Virology* **172,** 616–627
17. Taraporewala, Z., Chen, D., and Patton, J. T. (1999) *J. Virol.* **73,** 9934–9943
18. Laue, T. M., Shah, B. D., Ridgeway, T. M., and Pelletier, S. L. (1992) in *Analytical Ultracentrifugation in Biochemistry and Polymer Science* (Harding, S. E., Rowe, A. J., and Horton, J. C., eds) pp. 90–125, The Royal Society of Chemistry, Cambridge
19. Svedberg, T., and Pedersen, K. O. (1940) *The ultracentrifuge*, Oxford University Press, London
20. Laue, T. M., and Stafford, W. F. I. (1999) *Annu. Rev. Biophys. Biomol. Struct.* **28,** 75–100
21. Rivas, G., Stafford, W., and Minton, A. P. (1999) *Methods Companion Methods Enzymol.* **19,** 194–212
22. Schuck, P., and Braswell, E. H. (2000) in *Current Protocols in Immunology* (Coligan, J. E., Kruisbeek, A. M., Margulies, D. H., Shevach, E. M., and Strober, W., eds) pp. 18.8.1–18.8.22, John Wiley & Sons, Inc., New York, in press
23. Johnson, M. L., and Straume, M. (1994) in *Modern Analytical Ultracentrifugation* (Schuster, T. M., and Laue, T. M., eds) pp. 37–65, Birkhäuser, Boston
24. Lamm, O. (1929) *Ark. Mat. Astr. Fys.* **21B,** 1–4
25. Schuck, P., and Demeler, B. (1999) *Biophys. J.* **76,** 2288–2296
26. Claverie, J.-M., Dreux, H., and Cohen, R. (1975) *Biopolymers* **14,** 1685–1700
27. Schuck, P. (1998) *Biophys. J.* **75,** 1503–1512
28. Schuck, P., MacPhee, C. E., and Howlett, G. J. (1998) *Biophys. J.* **74,** 466–474
29. Poncet, D., Lindenbaum, P., L'Haridon, R., and Cohen, J. (1997) *J. Virology* **71,** 34–41
30. Schuck, P. (2000) *Biophys. J.* **78,** 1606–1619
31. Darawshe, S., Rivas, G., and Minton, A. P. (1993) *Anal. Biochem.* **209,** 130–135
32. Murphy, R. M. (1997) *Curr. Opin. Biotechnol.* **8,** 25–30
33. Provencher, S. W., and Glockner, J. (1981) *Biochemistry* **20,** 33–37
34. Kuntz, I. D. (1971) *J. Am. Chem. Soc.* **93,** 516–518
35. Perugini, M. A., Schuck, P., and Howlett, G. J. (2000) *J. Biol. Chem.* **275,** 36758–36765
36. Patton, J. T. (2001) *Gastroenteritis Viruses*, pp. 64–77, John Wiley & Sons, Chichester, United Kingdom
37. Soengas, M. S., Mateo, C. R., Rivas, G., Salas, M., Acuna, A. U., and Gutierrez, C. (1997) *J. Biol. Chem.* **272,** 303–310
38. Misselwitz, R., Welfle, K., Curth, U., Urbanke, C., and Welfle, H. (1995) *J. Biomol. Struct. Dyn.* **12,** 1041–1054
39. Tucker, P. A., Tsernoglou, D., Tucker, A. D., Coenjaerts, F. E., Leenders, H., and van der Vliet, P. C. (1994) *EMBO J.* **13,** 2994–3002
40. Folmer, R. H., Nilges, M., Konings, R. N., and Hilbers, C. W. (1995) *EMBO J.* **14,** 4132–4142
41. Passy, S. I., Yu, X., Li, Z., Radding, C. M., Masson, J.-Y., West, S. C., and Egelman, E. H. (1999) *Proc. Natl. Acad. Sci. U. S. A.* **96,** 10684–10688
42. Egelman, E. H., Yu, X., Wild, R., Hingorani, M. M., and Patel, S. S. (1995) *Proc. Natl. Acad. Sci. U. S. A.* **92,** 3869–3873
43. Curth, U., Urbanke, C., Greipel, J., Gerberding, H., Tiranti, V., and Zeviani, M. (1994) *Eur. J. Biochem.* **221,** 435–443
44. Raghunathan, S., Kozlov, A. G., Lohman, T. M., and Waksman, G. (2000) *Nat. Struct. Biol.* **7,** 648–652
45. Li, K., and Williams, R. S. (1997) *J. Biol. Chem.* **272,** 8686–8694
46. Genschel, J., Litz, L., Thole, H., Roemling, U., and Urbanke, C. (1996) *Gene* (*Amst.*) **182,** 137–143
47. Yang, C., Curth, U., Urbanke, C., and Kang, C. (1997) *Nat. Struct. Biol.* **4,** 153–157
48. Ferrari, M. E., Fang, J., and Lohman, T. M. (1997) *Biophys. Chem.* **64,** 235–251
49. Tseng, M., Palaniyar, N., Zhang, W., and Evans, D. H. (1999) *J. Biol. Chem.* **274,** 21637–21644
50. Lohman, T. M., and Ferrari, M. E. (1994) *Annu. Rev. Biochem.* **63,** 527–570